Detection of new sources of methanol emission at 95 GHz with the Mopra telescope

I. E. Val'tts,[1] S. P. Ellingsen,[2]★ V. I. Slysh,[1] S. V. Kalenskii,[1] R. Otrupcek[3] and G. M. Larionov[1]

[1]*Astro Space Center of Lebedev Physical Institute, Profsoyuznaya 84/32, 117810 Moscow, Russia*
[2]*School of Mathematics and Physics, University of Tasmania, GPO Box 252-21, Hobart 7001, TAS, Australia*
[3]*Australia Telescope National Facility, PO Box 76, Epping 2121, NSW, Australia*

ABSTRACT

A southern hemisphere survey of methanol emission sources has been carried out using the Australia Telescope National Facility Mopra millimetre telescope. 85 sources, the majority of them masers, have been detected in the 8_0-7_1 A^+ transition of methanol at 95 GHz. Together with a similar northern hemisphere survey, this completes the search for 95-GHz methanol emission from the Galactic plane. The previously found correlation between intensities of methanol emission at 44 and 95 GHz is confirmed here with the larger sample of sources. The results of large velocity gradient statistical equilibrium calculations confirm the classification of these sources as class I methanol masers pumped through collisional excitation.

Key words: masers – surveys – ISM: molecules – radio lines: ISM.

1 INTRODUCTION

Methanol, OH and H_2O masers are all frequently associated with massive star formation regions; however, methanol masers offer more possibilities for the study of star-forming regions than either OH or H_2O, because there are numerous transitions in the microwave region of the spectrum. One of the most widespread methanol masers is the 7_0-6_1 A^+ transition at 44 GHz. About 50 masers from this transition have been detected in the northern hemisphere (Morimoto, Ohishi & Kanzawa 1985; Haschick, Menten & Baan 1990; Bachiller et al. 1990; Kalenskii et al. 1992, 1994), and a similar number have been found in the southern hemisphere (Slysh et al. 1994). According to the empirical scheme of Menten (1991), the 44-GHz 7_0-6_1 A^+ transition is a class I methanol maser. Class I methanol masers differ from class II methanol masers in that they are not directly associated with compact H II regions and OH masers, and the two classes also emit in different transitions.

The 8_0-7_1 A^+ transition at 95 GHz is an analogue of the 44-GHz masing transition (see fig. 1 of Val'tts et al. 1999). The upper (8_0) energy level of the 95-GHz transition is 18.5 K higher than the upper (7_0) energy level of the 44-GHz transition, and modelling (Cragg et al. 1992) shows that strong maser emission is also expected from this transition. Val'tts et al. (1995) carried out a search for 95-GHz methanol masers with the Onsala radio telescope which detected a large number, mostly at the position of 44-GHz masers and with spectra similar to the spectra of the

44-GHz masers. The intensity of 95-GHz masers was found to correlate with the intensity of 44-GHz masers, and was on average about 0.5 of the intensity of 44-GHz masers. In this paper we present the results of the first search for 95-GHz methanol masers in the southern hemisphere, carried out with the Australia Telescope National Facility (ATNF) Mopra telescope in Australia. This search completes a whole-sky survey of class I methanol maser sources in two transitions, at 44 and 95 GHz.

2 OBSERVATIONS

The observations were carried out in the period from 1997 July 1 to 17, using the Mopra 22-m millimeter-wave telescope of the ATNF. The assumed rest frequency of the 8_0-7_1 A^+ transition of methanol was 95.169 489 GHz (De Lucia et al. 1989). At this frequency only the inner 15 m of the Mopra antenna is illuminated and the aperture efficiency is 41 per cent, which implies that 1 K of antenna temperature corresponds to 40 Jy. The half-power beamwidth of the Mopra antenna at 95 GHz is 52 arcsec. The observations were performed in a position-switching mode with reference positions offset 30 arcmin in declination. The antenna pointing was checked and corrected every 12 h by making observations of 86-GHz SiO masers; the nominal pointing accuracy when this procedure is followed is 10 arcsec rms. For the majority of sources, observations were made only at the nominal position, as time limitations did not permit the observation of grids at offset positions (to determine the position accurately) to be made. A grid of observations was made toward a

★ E-mail: simon.ellingsen@utas.edu.au

Table 1. Detected 95-GHz methanol sources. Gaussian parameters were determined from 64-MHz Hanning-smoothed spectra, except where noted. [a]Gaussian parameters determined from uniformly weighted spectrum; [b]Gaussian parameters determined from 32-MHz bandwidth spectrum; [c]detection only marginal. Distances were determined using the Galactic rotation curve model of Brand & Blitz (1993), except where otherwise noted. [1]Genzel & Stutzki (1989); [2]Sung, Bessell & Lee (1997); [3]Neckel (1978); [4]Houghton & Whiteoak (1995); [5]Thronson, Lowenstein & Stokes (1979).

Source	RA 1950 (h m s)	Dec. 1950 (° ′ ″)	Peak flux density (Jy)	LSR radial velocity (km s^{-1})	Line FWHM (km s^{-1})	Distance Near (kpc)	Far (kpc)
OMC-2[a,b]	05:32:59.80	−05:11:29.0	4(2)	10.9(0.2)	0.9(0.5)	0.45[1]	
			138(7)	11.4(0.01)	0.3(0.01)		
			85(7)	11.5(0.01)	0.7(0.03)		
NGC 2264[a,b]	06:38:24.90	09:32:28.0	99.2(5.7)	7.3(0.01)	0.2(0.02)	0.76[2]	
			55.2(3.7)	7.6(0.03)	0.7(0.04)		
269.20−1.13[a]	09:01:52.96	−48:16:07.1	15.1(2.3)	9.4(0.1)	0.7(0.1)	2.9	3.2
			6.5(1.5)	10.7(0.2)	1.6(0.6)		
270.26+0.84[a]	09:14:56.26	−47:43:34.1	7.0(3.1)	9.3(0.1)	0.6(0.4)	3.1	
			21.0(1.6)	9.8(0.1)	2.8(0.2)		
294.97−1.73	11:36:51.54	−63:12:09.4	5.9(0.8)	−8.2(0.1)	1.3(0.2)	0.6	6.6
300.97+1.15[a]	12:32:02.60	−61:23:06.0	9.4(1.2)	−42.2(0.05)	0.7(0.1)	4.2	
301.14−0.23[a]	12:32:42.60	−62:45:57.0	27.8(2.4)	−36.3(0.2)	1.5(0.3)	4.4	
			27.2(8.1)	−35.4(0.05)	0.6(0.1)		
305.21+0.21[a,b]	13:07:57.54	−62:18:44.2	62.1(2.5)	−42.4(0.01)	0.61(0.03)	4.9	
305.25+0.25[a]	13:08:20.50	−62:16:07.0	13.9(0.8)	−36.6(0.1)	1.4(0.1)	2.5	7.3
305.36+0.20[a]	13:09:21.00	−62:17:30.0	7.8(1.4)	−34.8(0.1)	0.9(0.2)	2.8	7.0
			17.4(1.4)	−33.4(0.4)	0.9(0.1)		
309.39−0.14	13:43:55.90	−62:03:14.0	5.6(0.8)	−51.0(0.3)	5.0(0.6)	2.2	8.5
			11.0(1.7)	−50.5(0.1)	0.7(0.1)		
316.76−0.02[a]	14:41:07.81	−59:35:33.1	12.9(1.6)	−39.4(0.1)	0.7(0.1)	2.7	9.7
320.28−0.31	15:06:25.71	−58:14:02.2	5.3(1.4)	−67.2(0.1)	0.5(0.2)	4.6	8.5
			14.5(1.9)	−66.3(0.02)	0.7(0.1)		
			9.5(0.6)	−65.1(0.2)	2.4(0.3)		
323.74−0.27	15:27:52.41	−56:20:48.1	4.3(1.0)	−52.5(0.1)	0.5(0.1)	3.3	10.4
			4.9(0.4)	−49.8(0.1)	2.9(0.3)		
324.72+0.34	15:31:06.71	−55:17:28.0	3.1(0.5)	−50.6(0.2)	2.5(0.4)	3.4	10.5
326.475+0.703	15:39:27.05	−53:57:42.5	4.4(2.2)	−41.5(0.5)	9.6(1.9)	2.6	11.6
			16.0(2.0)	−40.9(0.1)	3.9(0.4)		
			7.9(1.6)	−40.8(0.1)	0.7(0.2)		
326.641+0.612	15:40:43.44	−53:56:05.9	15.8(0.6)	−39.4(0.1)	4.3(0.2)	2.9	11.3
327.392+0.199	15:46:27.84	−53:48:01.7	5.7(0.5)	−89.4(0.1)	1.1(0.2)	5.3	9.0
			3.7(0.6)	−88.3(0.2)	0.8(0.3)		
326.859−0.667	15:47:20.40	−54:49:03.6	8.9(0.7)	−67.1(0.1)	1.9(0.2)	3.7	10.5
327.618−0.111	15:48:58.76	−53:54:05.4	6.0(0.5)	−88.2(0.04)	1.3(0.1)	6.5	7.9
327.29−0.58	15:49:13.01	−54:28:12.1	9.8(2.3)	−47.2(0.4)	3.0(0.5)	3.0	11.3
			14.3(1.1)	−44.6(0.2)	2.5(0.9)		
			5.1(1.6)	−42.0(0.8)	3.5(1.1)		
328.81+0.64	15:52:00.01	−52:34:03.9	3.6(1.6)	−43.0(0.2)	1.6(0.6)	2.9	11.6
			1.2(1.1)	−42.0(0.2)	0.6(0.6)		
			1.3(0.9)	−41.0(0.2)	0.9(0.7)		
			7.2(0.9)	−40.9(0.3)	3.1(0.4)		
328.24−0.55	15:54:06.12	−53:50:47.1	2.7(0.6)	−44.0(0.2)	1.1(0.5)	2.8	11.6
			4.0(0.9)	−42.9(0.1)	0.8(0.3)		
			7.3(0.4)	−41.2(0.1)	1.8(0.2)		
329.469+0.502	15:55:52.44	−52:14:58.0	3.7(0.7)	−69.5(0.5)	2.4(0.8)	4.5	10.1
			4.5(0.6)	−66.7(0.4)	3.1(0.7)		
			2.3(0.7)	−63.4(0.1)	0.8(0.3)		
329.03−0.21[a]	15:56:42.01	−53:04:22.1	19.3(1.3)	−43.7(0.1)	1.3(0.1)	3.1	11.4
			10.3(3.3)	−42.5(0.1)	0.5(0.2)		
			12.5(1.6)	−41.7(0.1)	0.9(0.3)		
			9.5(1.5)	−40.5(0.1)	0.9(0.3)		
329.066−0.308	15:57:18.97	−53:07:38.5	2.2(0.4)	−42.2(0.3)	4.3(0.9)	3.0	11.6
			2.6(0.9)	−42.0(0.1)	0.5(0.2)		
329.183−0.314	15:57:56.13	−53:03:22.4	7.0(0.3)	−49.8(0.1)	2.2(0.2)	3.6	11.0
			2.5(0.5)	−47.5(0.2)	1.6(0.4)		
331.13−0.25	16:07:11.01	−51:42:53.1	20.5(0.7)	−91.0(0.02)	1.0(0.04)	5.5	9.4
			5.7(0.4)	−88.5(0.2)	2.8(0.5)		
			5.7(0.4)	−84.8(0.2)	3.0(0.4)		
331.442−0.187	16:08:24.07	−51:27:28.6	4.4(0.6)	−91.5(0.1)	0.4(0.2)	5.4	9.6
			3.9(0.6)	−87.9(0.1)	1.1(0.2)		
331.34−0.35[a]	16:08:37.41	−51:38:32.1	15.8(1.3)	−65.7(0.03)	0.7(0.1)	4.2	10.7
332.295−0.094	16:11:58.11	−50:48:26.0	4.9(1.9)	−49.6(0.1)	0.6(0.2)	3.2	11.8
			3.2(0.6)	−48.8(0.3)	1.2(0.6)		
332.604−0.167[a]	16:13:42.20	−50:38:51.4	8.8(0.9)	−45.8(0.04)	0.9(0.1)	3.5	11.6
333.23−0.05[a]	16:16:02.01	−50:07:50.1	26.3(1.0)	−87.2(0.03)	1.2(0.1)	5.3	9.9

Table 1 – *continued*

Source	RA 1950 (h m s)	Dec. 1950 (° ′ ″)	Peak flux density (Jy)	LSR radial velocity (km s⁻¹)	Line FWHM (km s⁻¹)	Distance Near (kpc)	Far (kpc)
			2.9(1.7)	−86.2(0.2)	0.7(0.4)		
333.13−0.43	16:17:13.01	−50:28:18.1	4.7(0.3)	−55.7(0.1)	2.2(0.3)	3.4	11.7
			7.4(0.5)	−53.1(0.1)	1.8(0.3)		
			4.17(0.6)	−51.4(0.2)	0.9(0.6)		
			4.30(1.1)	−50.6(0.1)	0.5(0.1)		
			11.3(0.4)	−48.5(0.1)	3.1(0.2)		
333.61−0.22[c]	16:18:25.01	−49:59:08.1	3.0(0.4)	−49.7(0.2)	2.9(0.4)	3.4	11.8
335.59−0.29[a]	16:27:15.40	−48:37:20.1	6.8(2.3)	−47.5(0.1)	0.9(0.3)	3.3	12.2
			10.2(2.4)	−46.6(0.2)	4.7(0.6)		
			6.8(2.6)	−46.3(0.1)	0.5(0.2)		
			22.3(2.2)	−45.5(0.03)	0.6(0.1)		
336.41−0.26	16:30:31.51	−48:00:08.1	6.6(0.7)	−89.7(0.1)	1.4(0.2)	5.3	10.3
			24.8(0.9)	−87.6(0.01)	0.7(0.03)		
337.40−0.41[a]	16:35:08.01	−47:22:23.1	9.4(2.1)	−44.2(0.1)	0.4(0.1)	3.3	12.4
			16.5(2.4)	−42.3(0.1)	0.2(0.1)		
			5.7(0.5)	−40.7(0.3)	7.4(0.8)		
338.92+0.56[a]	16:36:54.01	−45:36:05.0	18.4(1.8)	−62.9(0.1)	1.1(0.1)	4.4	11.5
			8.3(1.4)	−60.1(0.2)	1.5(0.4)		
337.91−0.47[a]	16:37:27.01	−47:02:10.1	58.2(2.4)	−43.6(0.01)	0.4(0.02)	3.3	12.4
341.19−0.22	16:48:39.50	−44:23:33.5	6.1(0.9)	−42.0(0.1)	0.7(0.1)	3.5	12.6
341.22−0.21[a]	16:48:42.10	−44:21:53.0	15.6(1.0)	−43.8(0.1)	1.8(0.1)	3.5	12.5
			6.4(2.2)	−43.0(0.1)	0.4(0.2)		
345.01+1.79[a,b]	16:53:21.00	−40:09:40.0	25.6(1.1)	−13.6(0.04)	2.8(0.1)	1.6	14.8
			42.0(1.9)	−13.1(0.01)	0.5(0.03)		
343.12−0.06[a]	16:54:43.00	−42:47:49.0	46.6(3.0)	−32.8(0.02)	0.8(0.1)	3.1	13.2
			24.3(2.9)	−31.5(0.02)	0.5(0.1)		
			22.1(1.9)	−31.2(0.2)	2.4(0.2)		
			19.7(1.5)	−27.3(0.02)	0.7(0.1)		
344.23−0.57[a]	17:00:35.16	−42:14:29.7	12.0(0.8)	−21.7(0.1)	3.9(0.3)	2.2	14.1
			33.2(1.9)	−20.3(0.02)	0.6(0.1)		
345.51+0.35	17:00:54.00	−40:40:02.0	4.6(0.3)	−17.1(0.1)	4.1(0.2)	2.0	14.4
			3.2(0.5)	−16.5(0.1)	0.9(0.2)		
			2.3(0.6)	−14.7(0.1)	0.5(0.1)		
345.00−0.22	17:01:38.51	−41:24:59.0	10.0(1.2)	−28.9(0.03)	0.6(0.1)	3.0	13.5
			10.0(1.2)	−28.0(0.1)	3.2(0.4)		
			23.5(1.4)	−28.0(0.02)	0.7(0.1)		
			3.4(1.1)	−26.0(0.6)	10.2(1.7)		
			10.6(0.8)	−23.9(0.03)	1.2(0.1)		
349.10+0.11	17:13:01.00	−37:56:06.0	6.4(1.6)	−78.0(0.1)	0.5(0.2)	6.0	10.7
			4.4(0.9)	−77.3(0.2)	2.3(0.4)		
351.16+0.70[a]	17:16:35.51	−35:54:44.0	22.2(5.9)	−7.2(0.5)	2.4(0.6)	1.4	15.4
			8.0(3.7)	−7.1(0.1)	0.3(0.2)		
			11.8(8.6)	−5.8(0.3)	1.1(0.5)		
			26.3(3.3)	−4.9(0.03)	0.6(0.1)		
351.24+0.67	17:16:54.51	−35:51:58.0	4.3(0.4)	−4.5(0.1)	3.4(0.3)	0.1	16.1
351.41+0.64[a]	17:17:32.35	−35:44:04.2	20.2(1.0)	−8.2(0.2)	4.2(0.3)	1.7[3]	
			7.0(1.3)	−6.4(0.1)	0.7(0.2)		
			6.6(1.6)	−4.6(0.5)	3.6(0.8)		
NGC 6334I(N)[a]	17:17:33.00	−35:42:04.0	42.6(4.0)	−7.5(0.03)	0.9(0.1)	1.7[3]	
			75.9(7.0)	−4.8(0.04)	1.7(0.2)		
			77.9(5.7)	−4.8(0.01)	0.3(0.03)		
			50.2(6.4)	−4.2(0.2)	5.4(0.3)		
			52.7(4.1)	−3.0(0.03)	0.8(0.1)		
351.78−0.54[a]	17:23:20.67	−36:06:45.4	23.0(1.9)	−8.3(0.02)	0.5(0.1)	1.5	15.3
			36.0(2.2)	−7.5(0.03)	0.5(0.1)		
			73.0(2.3)	−6.9(0.01)	0.4(0.03)		
			26.8(1.2)	−3.9(0.1)	7.1(0.2)		
			51.6(2.3)	−2.4(0.01)	0.4(0.02)		
			22.2(1.6)	−2.0(0.1)	2.4(0.2)		
351.64−1.26	17:25:55.00	−36:37:48.0	10.2(1.2)	−13.0(0.1)	1.2(0.2)	2.5	14.3
354.61+0.47[a]	17:27:00.00	−33:11:38.0	9.6(2.1)	−21.4(0.04)	0.4(0.1)	4.0	12.9
			7.8(0.8)	−20.5(0.2)	3.0(0.3)		
			24.0(1.7)	−17.9(0.02)	0.5(0.04)		
353.41−0.36	17:27:07.00	−34:39:41.0	6.5(0.4)	−17.4(0.1)	5.0(0.3)	3.4	13.5
			8.1(0.8)	−16.6(0.03)	0.6(0.1)		
SgrA-F[a]	17:42:27.40	−29:02:18.0	8.9(0.4)	17.8(0.7)	2.1(1.1)		
			4.1(1.2)	23.9(0.3)	4.2(1.1)		
359.62−0.25	17:42:30.00	−29:22:31.0	5.3(0.7)	17.7(0.1)	1.7(0.3)		
			15.9(1.1)	19.3(0.03)	0.6(0.1)		
			9.0(0.8)	20.6(0.1)	1.2(0.1)		

Table 1 – *continued*

Source	RA 1950 (h m s)	Dec. 1950 (° ′ ″)	Peak flux density (Jy)	LSR radial velocity (km s^{-1})	Line FWHM (km s^{-1})	Distance Near (kpc)	Distance Far (kpc)
Sgr A-A[a]	17:42:41.30	−28:58:18.0	12.1(0.2)	42.1(0.2)	18.3(0.4)		
Sgr B2[a]	17:44:10.60	−28:22:05.0	34.1(4.3)	59.0(1.9)	14.4(4.2)	8.5[4]	
			7.8(0.3)	70.5(3.4)	8.2(9.0)		
0.54−0.85	17:47:04.10	−28:54:01.0	4.1(0.9)	15.2(0.2)	2.3(0.4)	7.5	9.5
			4.0(0.9)	16.9(0.1)	0.6(0.2)		
			4.7(0.3)	18.3(0.4)	4.1(0.7)		
5.89−0.39[a]	17:57:26.80	−24:03:54.0	9.5(0.8)	8.5(0.1)	1.2(0.1)	2.4	14.5
			6.1(0.5)	9.6(0.2)	7.7(0.5)		
			9.2(1.3)	11.6(0.03)	0.4(0.1)		
			9.7(2.5)	12.3(0.03)	0.3(0.1)		
M8E[a,b]	18:01:49.71	−24:26:56.0	129.7(2.0)	11.0(0.01)	0.5(0.01)	1.78[5]	
8.67−0.36	18:03:19.00	−21:37:59.0	4.9(0.7)	33.5(0.3)	1.5(0.5)	4.5	12.3
			5.9(1.2)	35.0(0.2)	1.2(0.4)		
			4.3(1.0)	36.2(0.1)	0.6(0.2)		
IRAS 18056−1952	18:05:38.00	−19:52:34.0	9.5(0.9)	61.7(0.02)	0.4(0.1)	5.8	10.9
10.6−0.4	18:07:30.50	−19:56:28.0	8.1(0.9)	−7.6(0.3)	2.2(0.4)	2.0	18.7
			7.3(2.2)	−6.4(0.1)	1.2(0.2)		
			3.9(0.6)	−4.7(0.1)	1.0(0.2)		
			4.1(0.5)	−2.8(0.1)	1.7(0.3)		
			3.2(0.3)	−1.4(0.7)	9.6(0.9)		
12.89+0.49[b]	18:08:56.40	−17:32:14.0	6.0(1.2)	29.6(0.04)	0.4(0.1)	3.5	13.1
			5.7(1.1)	31.5(0.1)	0.4(0.2)		
			5.1(0.4)	32.9(0.2)	3.3(0.4)		
11.94−0.62	18:11:04.40	−18:54:20.0	3.1(0.5)	35.0(0.1)	1.4(0.2)	3.9	12.7
			2.7(0.6)	36.8(0.1)	0.6(0.2)		
			5.5(0.4)	38.5(0.1)	1.3(0.1)		
W33MetC[a]	18:11:15.70	−17:56:53.0	21.2(3.1)	32.7(0.04)	0.5(0.1)	3.4	13.2
IRAS 18141−1615	18:14:09.00	−16:15:47.0	4.0(1.1)	21.9(0.1)	0.8(0.3)	2.1	14.4
			3.7(0.7)	23.1(0.3)	0.8(1.0)		
			7.2(1.0)	25.0(0.2)	2.1(0.4)		
IRAS 18151−1208	18:15:09.00	−12:08:34.0	3.3(0.4)	32.2(0.1)	1.3(0.2)	2.8	13.4
			3.9(0.7)	33.9(0.1)	0.6(0.1)		
14.33−0.64[a]	18:16:00.80	−16:49:06.0	38.9(1.8)	19.1(0.02)	0.9(0.1)	2.6	13.9
			32.2(2.0)	20.4(0.03)	0.7(0.1)		
			11.8(2.3)	21.3(0.1)	0.7(0.2)		
			50.1(1.8)	22.5(0.02)	1.0(0.1)		
			52.8(2.9)	23.4(0.02)	0.5(0.04)		
GGD 27[a,b]	18:16:13.80	−20:48:31.0	19.3(2.7)	12.4(0.02)	0.3(0.1)	2.1	14.6
			33.4(3.9)	12.9(0.02)	0.3(0.04)		
			76.2(2.8)	13.3(0.01)	0.4(0.03)		
			14.8(3.2)	13.7(0.02)	0.2(0.1)		
M17(3)	18:17:31.00	−16:12:50.0	1.9(1.9)	19.0(1.2)	2.0(1.6)	2.2	14.2
			2.8(3.0)	19.1(0.1)	0.4(0.2)		
			2.8(0.5)	19.4(0.3)	5.4(0.7)		
16.59−0.06	18:18:20.30	−14:33:18.0	5.7(1.1)	60.4(0.2)	1.1(0.4)	4.7	11.6
			9.8(1.6)	61.3(0.1)	0.8(0.2)		
19.61−0.23[a]	18:24:50.30	−11:58:34.0	6.2(0.7)	41.3(0.1)	1.9(0.3)	3.4	12.6
L379IRS3	18:26:32.90	−15:17:58.0	3.9(0.8)	17.8(0.3)	9.2(1.2)	1.7	14.6
			4.6(1.3)	17.7(0.1)	0.7(0.2)		
			10.1(1.2)	18.0(0.1)	2.7(0.3)		
			6.0(0.8)	20.3(0.1)	0.9(0.2)		
23.43−0.19[a]	18:31:55.80	−08:34:17.0	7.0(1.4)	96.6(0.2)	1.7(0.4)	5.8	9.8
			33.8(2.5)	99.6(0.02)	0.5(0.04)		
23.01−0.41[c]	18:31:56.70	−09:03:18.0	3.4(0.6)	77.4(0.1)	1.3(0.3)	4.9	10.8
29.96−0.02	18:43:27.10	−02:42:36.0	3.3(0.6)	96.2(0.1)	0.7(0.2)	6.1	8.6
			3.8(0.6)	97.1(0.1)	0.7(0.2)		
			3.2(0.5)	98.7(0.1)	1.1(0.2)		
			2.8(0.7)	100.4(0.1)	0.9(0.2)		
30.69−0.06	18:44:58.90	−02:04:27.0	3.2(0.3)	91.4(0.2)	5.0(0.4)	5.3	9.3
			3.8(0.7)	93.1(0.1)	0.6(0.2)		
IRAS 18537+0749[a]	18:53:46.00	07:49:16.0	5.9(1.1)	30.0(0.3)	1.6(0.6)	2.2	10.8
			26.7(2.2)	31.5(0.1)	0.9(0.2)		
			22.3(5.0)	32.3(0.1)	0.6(0.2)		
			18.4(1.3)	33.3(0.1)	1.5(0.2)		
35.05−0.52[a]	18:54:37.10	01:35:01.0	16.1(1.1)	49.9(0.02)	0.7(0.1)	3.3	10.6
W51e1/e2	19:21:26.20	14:54:43.0	17.7(0.5)	55.9(0.1)	5.3(0.2)	5.4	
			4.8(0.7)	61.1(0.2)	2.6(0.5)		
W51Met2[a,b]	19:21:28.90	14:23:48.0	10.5(2.0)	54.2(0.1)	1.0(0.2)	5.5	
			19.7(2.6)	56.7(0.04)	0.6(0.1)		

number of interesting sources, and for some cases where the 95-GHz emission was anomalously low. A number of these grids found the strongest emission to be offset from the nominal position, and in some cases this will be due to antenna pointing errors. However, many of the sources have only been observed in lower frequency class I transitions, and the offset may be due to the limited accuracy to which the source position has been previously determined.

A cryogenically cooled low-noise SIS mixer was used in the receiver. The single-sideband receiver noise temperature was 110 K and the system temperature varied between 220 and 320 K depending on weather conditions and the elevation of the telescope. An ambient temperature load (assumed to have a temperature of 290 K) was regularly placed in front of the receiver to enable calibration using the method of Kutner & Ulich (1981). This corrects the observed flux density for the effects of atmospheric absorption, ohmic losses and rear-ward spillover. Variations in the ambient temperature of a few per cent occurred during the observations, and the estimated uncertainty of the absolute flux density scale is 10 per cent.

For the majority of the observations the back-end was a 64 MHz wide 1024-channel autocorrelator with a frequency resolution of 62.5 kHz. This yields a velocity resolution at 95 GHz of $0.236 \, \mathrm{km \, s^{-1}}$ with uniform weighting and $0.394 \, \mathrm{km \, s^{-1}}$ with Hanning smoothing. Some sources were re observed with the correlator configured to a 32-MHz bandwidth, also with 1024 spectral channels. This yields a velocity resolution of $0.118 \, \mathrm{km \, s^{-1}}$ with uniform weighting and $0.197 \, \mathrm{km \, s^{-1}}$ with Hanning smoothing. For each source a uniformly weighted spectrum was produced with a velocity width of approximately $80 \, \mathrm{km \, s^{-1}}$ centred on the velocity of the previously detected class I or II methanol maser emission. The spectrum was then Hanning smoothed to improve the signal-to-noise ratio of weak sources. For the Mopra observations, the spectra in all figures and Gaussian parameters (peak flux density, velocity and full width to half-maximum) in all tables are Hanning-smoothed data collected with the 64-MHz correlator configuration, unless otherwise noted in Table 1.

The source list was compiled primarily from 44-GHz class I methanol masers detected in the southern hemisphere by Slysh et al. (1994) and Haschick et al. (1990). The observing list also included 12 class I methanol masers detected at 36 GHz at Puschino (Kalenskii, private communication), 55 class II methanol sources that had not previously been searched for class I maser emission (Caswell et al. 1995; Ellingsen et al. 1996 and in preparation; Walsh et al. 1997) and 12 H II regions for which no 44-GHz emission was detected by Slysh et al. (1994).

3 RESULTS

A total of 153 sites were searched for 95-GHz methanol emission, with detections observed toward 85. Table 1 contains a list of all detected sources along with the Gaussian parameters of their spectral features. Their spectra are shown in Fig. 1. The sources toward which no 95-GHz emission was detected are listed in Table 2, along with the 3σ limit (typically less than 5 Jy). The kinematic distance to each source was estimated using the rotation curve of Brand & Blitz (1993). For many of the sources the model yields two distance estimates. The majority are likely to be at the nearer distance, but we have not attempted to resolve the ambiguity, and where it occurs both distances are listed in Tables 1 and 2. 86 known 44- or 36-GHz class I methanol sources were

observed, with 95-GHz emission being detected toward 71 (83 per cent). A total of 54 class II methanol maser sites that had not previously been searched for class I methanol emission were also observed, yielding a total of 13 detections (24 per cent).

79 of the 85 sources in Table 1 are new detections; the other six were discovered previously by Val'tts et al. (1995) at Onsala. In Table 3 we compare the Gaussian parameters of the strongest features of six sources observed at both Onsala and Mopra. The radial velocities agree within $0.4 \, \mathrm{km \, s^{-1}}$ in all cases, which is approximately half the spectral resolution of the Onsala observations. The flux densities agree to within a factor of 2, which is reasonable, taking into account differences in the spectral resolution, absolute calibration and possible pointing errors. Examination of Table 3 shows that some of the masers (e.g. OMC-2 and NGC 2264) have very narrow lines of $0.2 \, \mathrm{km \, s^{-1}}$, which were completely unresolved with the $0.7 \, \mathrm{km \, s^{-1}}$ spectral resolution of the Onsala observations. The Onsala results have not been corrected for spectral smoothing, and for this reason very narrow features in OMC-2, NGC 2264 and W51Met2 will have lower peak flux density than that observed at Mopra. Below we give comments for some of the more interesting sources.

3.1 Comments on individual sources

OMC-2. The 95-GHz methanol maser in this source consists of a very intense narrow line similar to that observed at 44 GHz (Haschick et al. 1990). The peak flux densities at both frequencies are almost equal, as are the line widths.

NGC 2264. This source shows an intense narrow line at 95 GHz with a shoulder on the positive velocity side. The spectrum of the 95-GHz methanol maser is very similar to that at 44 GHz, but the peak flux density is a factor of 2 lower.

305.21+0.21. The spectra of the 95- and 44-GHz masers are very similar, showing a single intense narrow line with the 95-GHz flux density only 25 per cent lower than the 44-GHz flux density.

333.13−0.43. The spectrum of this source in Fig. 1 shows a weak broad line. Comparing this spectrum, with the 44-GHz spectrum we suspected that 95-GHz flux density was too low, possibly because of a pointing error. To check this we made a five-point map consisting of observations at the central position and offset by ± 20 arcsec in both right ascension and declination. Fig. 2 contains the spectra from this map, which show that the strongest emission is offset to the south-west of the nominal position and that there are at least two rather strong narrow lines, confirming that this is a maser.

333.23−0.05. This source (Fig. 1) has an intense isolated spectral feature, which is best fitted by two Gaussians. A five-point map (Fig. 3) shows that the source is in fact offset from the nominal position by approximately -20 arcsec in right ascension. The 95-GHz maser spectrum is similar to that at 44 GHz, where it is a factor of 3 stronger.

335.59−0.29. The 95-GHz spectrum of this source is best fitted with four Gaussian components, while at 44 GHz only one intense component is present at the same radial velocity as the strongest 95-GHz component.

337.91−0.47. The 95-GHz methanol maser spectrum is essentially identical to the 44-GHz spectrum, but the peak flux density at 44 GHz is a factor of 4 higher.

338.92+0.56. The 95-GHz spectrum of this source has two narrow features, at radial velocities -62.9 and $-60.1 \, \mathrm{km \, s^{-1}}$, the
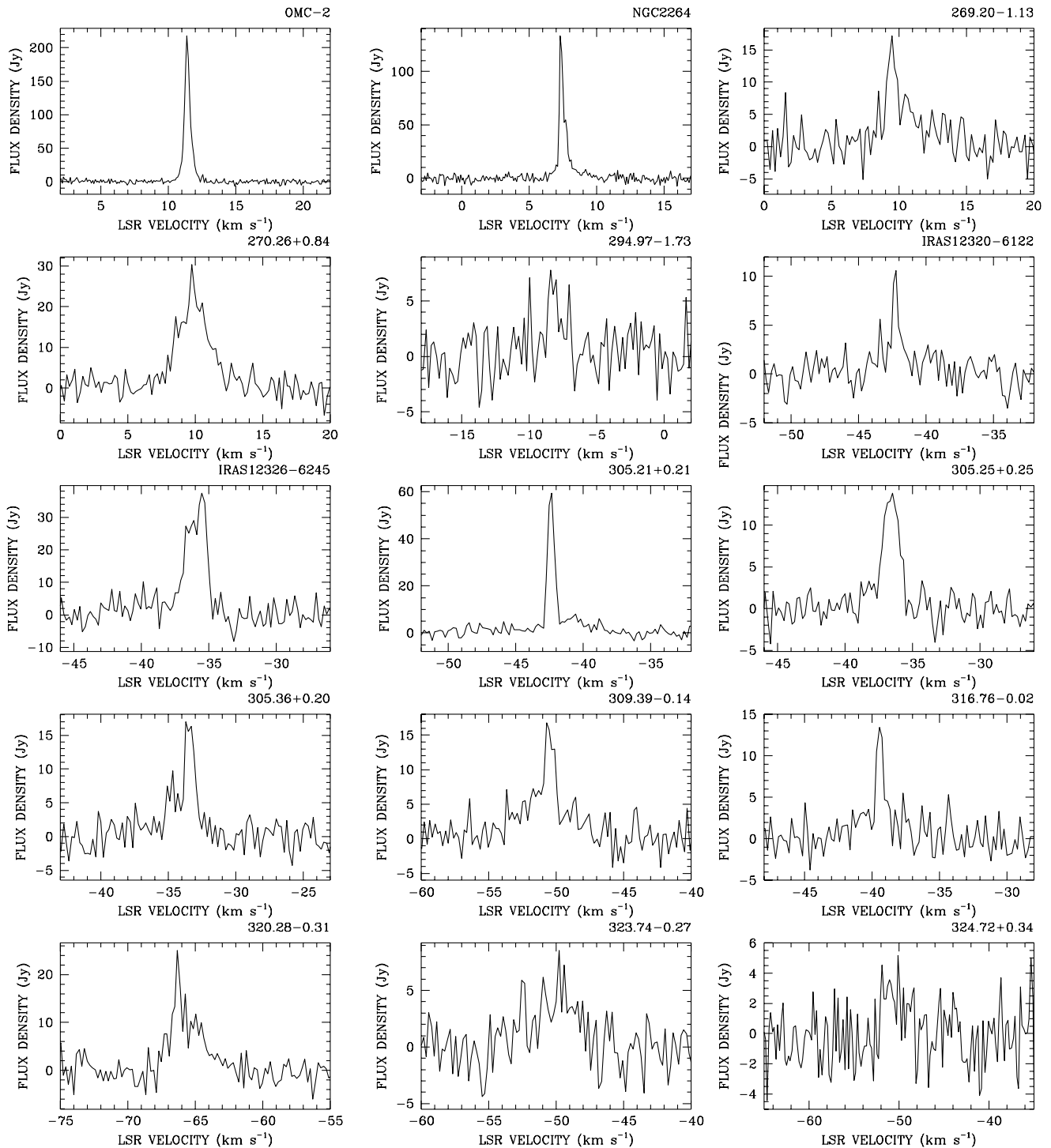
Figure 1. 95-GHz spectra. All spectra are Hanning smoothed.

same as the 44-GHz spectrum (Slysh et al. 1994). However, a five-point map centred on the nominal position of the source (Fig. 4) shows that the strongest emission is to the north, where the flux density is at least a factor of 2 higher. From the spectrum of the offset (0, 20 arcsec) one can see also a third detail, at a radial velocity of $-65.2\,\mathrm{km\,s^{-1}}$, which is not present in the 44-GHz spectrum. The five-point map also shows that the position of the spectral feature at $-60.1\,\mathrm{km\,s^{-1}}$ is shifted in right ascension relative to the spectral feature at $-62.9\,\mathrm{km\,s^{-1}}$ by about 20 arcsec.

343.12−0.06. The 95-GHz spectrum of this source has been fitted with four Gaussian components, all of which have counterparts in the 44-GHz spectrum (Slysh et al. 1994), although the relative intensities are different at the two frequencies. A five-point map of the source (Fig. 5) shows that the emission in the source consists of components separated by at least 20 arcsec, so the difference in relative intensities is most likely due to the different telescope beamwidths and pointing errors between the 44- and 95-GHz observations.
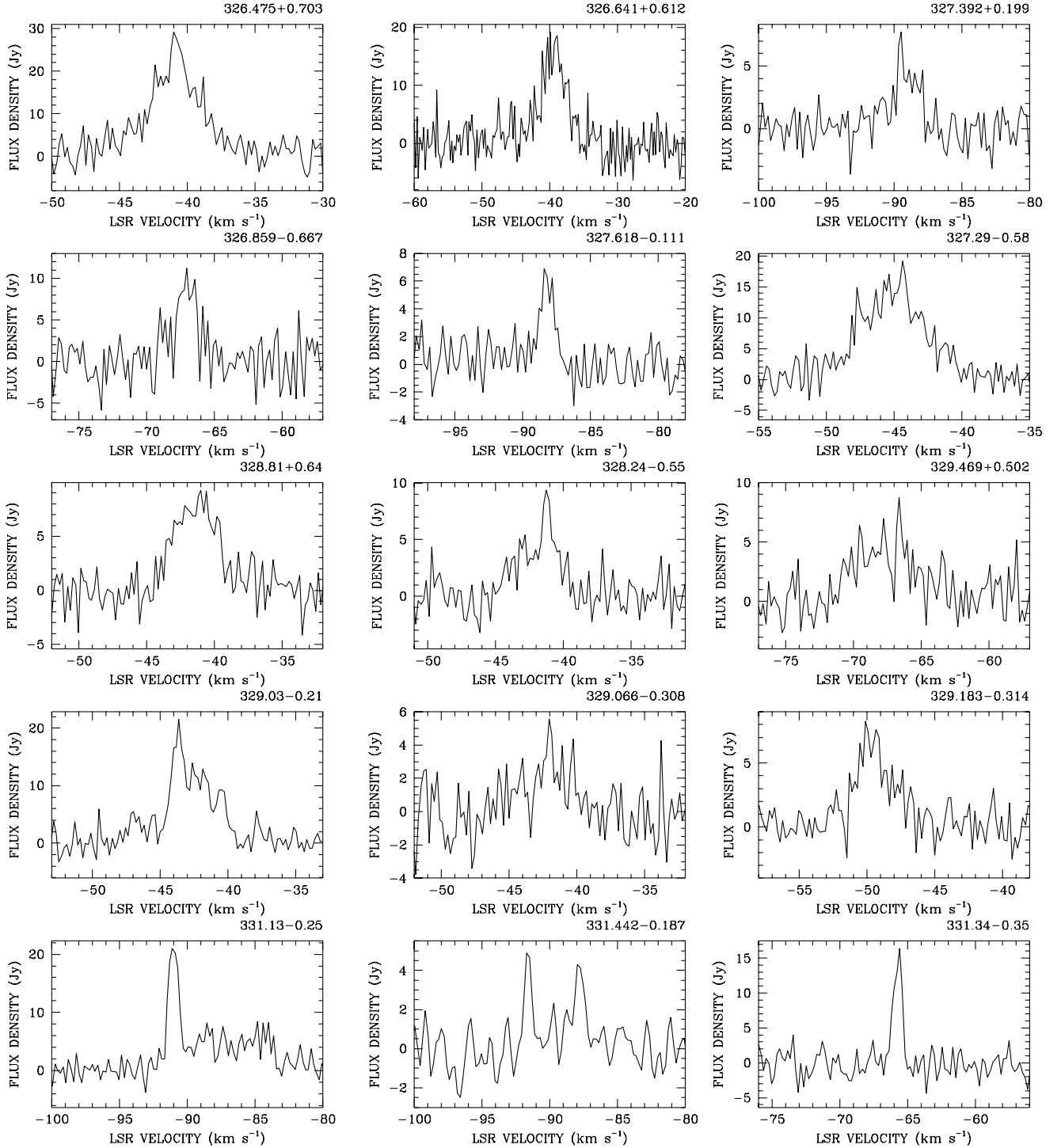
Figure 1 – *continued*

345.01+1.79. The 95-GHz spectrum of this source has been fitted by two Gaussians separated by $1.2\,\mathrm{km\,s^{-1}}$. A nine-point map of this source (Val'tts 1998) was used to determine the positions of both components. The stronger component at $-13.1\,\mathrm{km\,s^{-1}}$ has a position which coincides within the errors with the position of the southern 6.7-GHz methanol maser (Norris et al. 1993). The weaker component at $-14.3\,\mathrm{km\,s^{-1}}$ is displaced from the stronger one by $-6.6 \pm 7.9\,\mathrm{arcsec}$ in right ascension and $10.2 \pm 5.3\,\mathrm{arcsec}$ in declination, and coincides within the errors with the position of the

northern 6.7-GHz methanol maser. Thus 95-GHz methanol masers are present in both regions of methanol maser emission in this source.

345.00−0.22. The 95-GHz methanol maser spectrum is similar to that at 44 GHz, except for the presence of an additional feature at $-24\,\mathrm{km\,s^{-1}}$, which is absent from the 44-GHz spectrum.

351.16+0.70 (NGC 6334B). The 95-GHz spectrum is similar to the 44-GHz spectrum, although, owing to blending of spectral features, the number of Gaussian components that we are able to fit is different, four at 95 GHz compared with seven at 44 GHz.
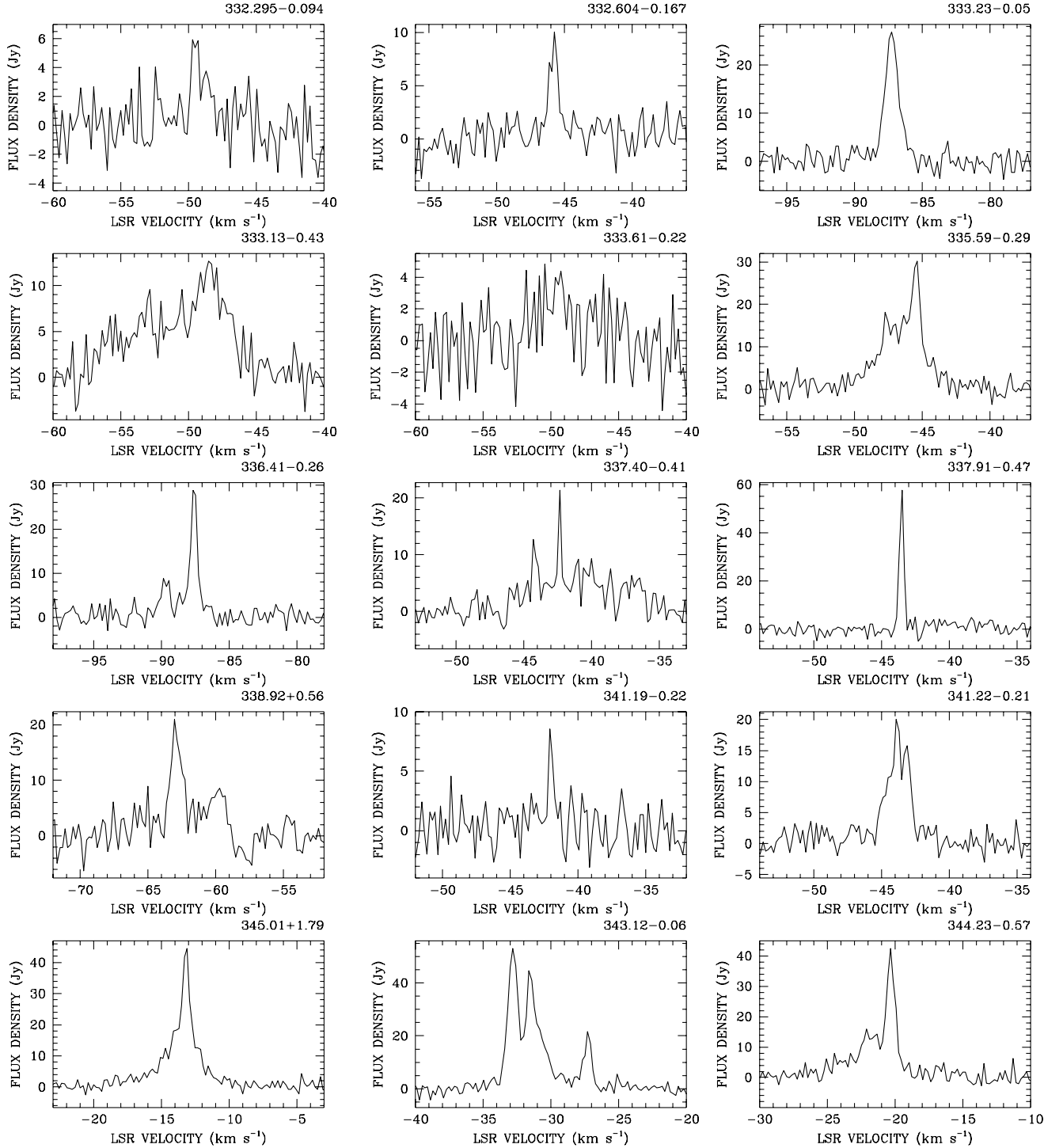
Figure 1 – *continued*

351.24+0.67 (NGC 6334C). The 95-GHz emission from this source is anomalously low compared with the 44-GHz emission (Slysh et al. 1994), possibly owing to poor pointing, or variable weather conditions.

351.41+0.64 (NGC 6334F). A broad line with some weaker narrow features is present in the 95-GHz spectrum; we have fitted the profile with two broad components and one narrow one at the radial velocity of $-6.4\,\mathrm{km\,s^{-1}}$. It is probably the counterpart of the $-6.32\,\mathrm{km\,s^{-1}}$ component in the 44-GHz spectrum (Slysh et al.

1994), but other narrow 44-GHz features are not present in the 95-GHz spectrum.

NGC 6334I(N). This is one of the strongest methanol masers at both 95 and 44 GHz (Haschick et al. 1990). The spectra are similar at the two frequencies, considering likely differences in pointing, since the maser is known to consist of components separated by more than 30 arcsec as can be seen from our map (Fig. 6). The relative positions of the four strongest spectral features were determined from this map and are given in Table 4. A comparison
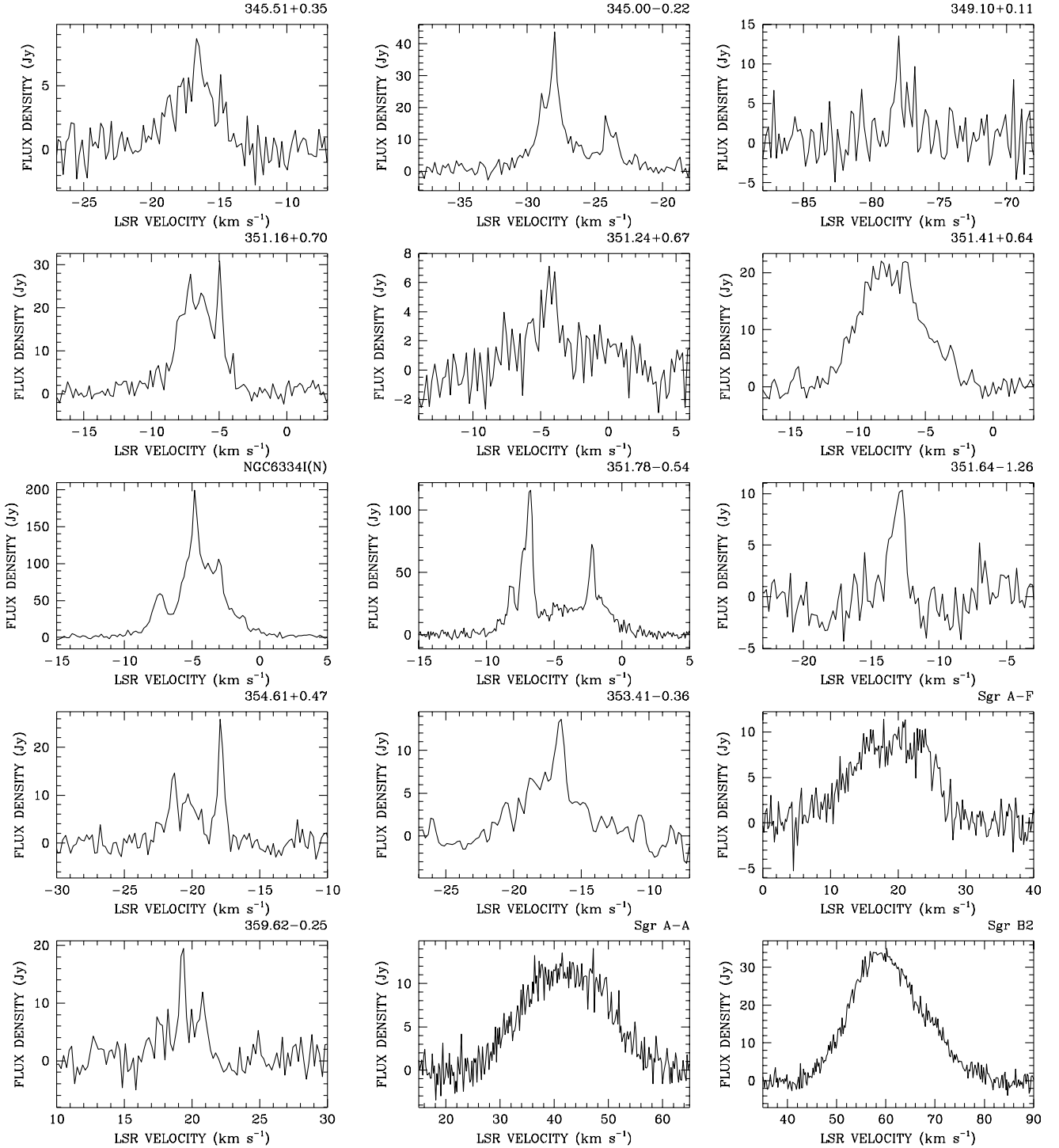
Figure 1 – *continued*

with the map of the source at 44 GHz (Kogan & Slysh 1998) shows that there is a general agreement between the two maps if the larger position errors of the 95-GHz map are taken into account. All four spectral features are point-like within the Mopra beamwidth of 52 arcsec.

351.64−1.26. A five-point map of this source shows that the single weak feature becomes stronger at offsets of (−20 arcsec, 0) and (0, −20 arcsec) (Fig. 7), which implies that the true source position is to the south-east of the the nominal position.

351.78−0.54. The 95-GHz spectrum consists of four narrow components, all of which are present in the 44-GHz spectrum, and in addition there is a broad component about 8 km s^{-1} wide, which is absent at 44 GHz.

354.61+0.47. At least three Gaussian components can be fitted to the 95-GHz spectrum of this source, and two of them are present in the 44-GHz spectrum. The component at −21.4 km s^{-1} is relatively stronger at 95 GHz, and the component at −20.5 km s^{-1} is present only at 95 GHz.
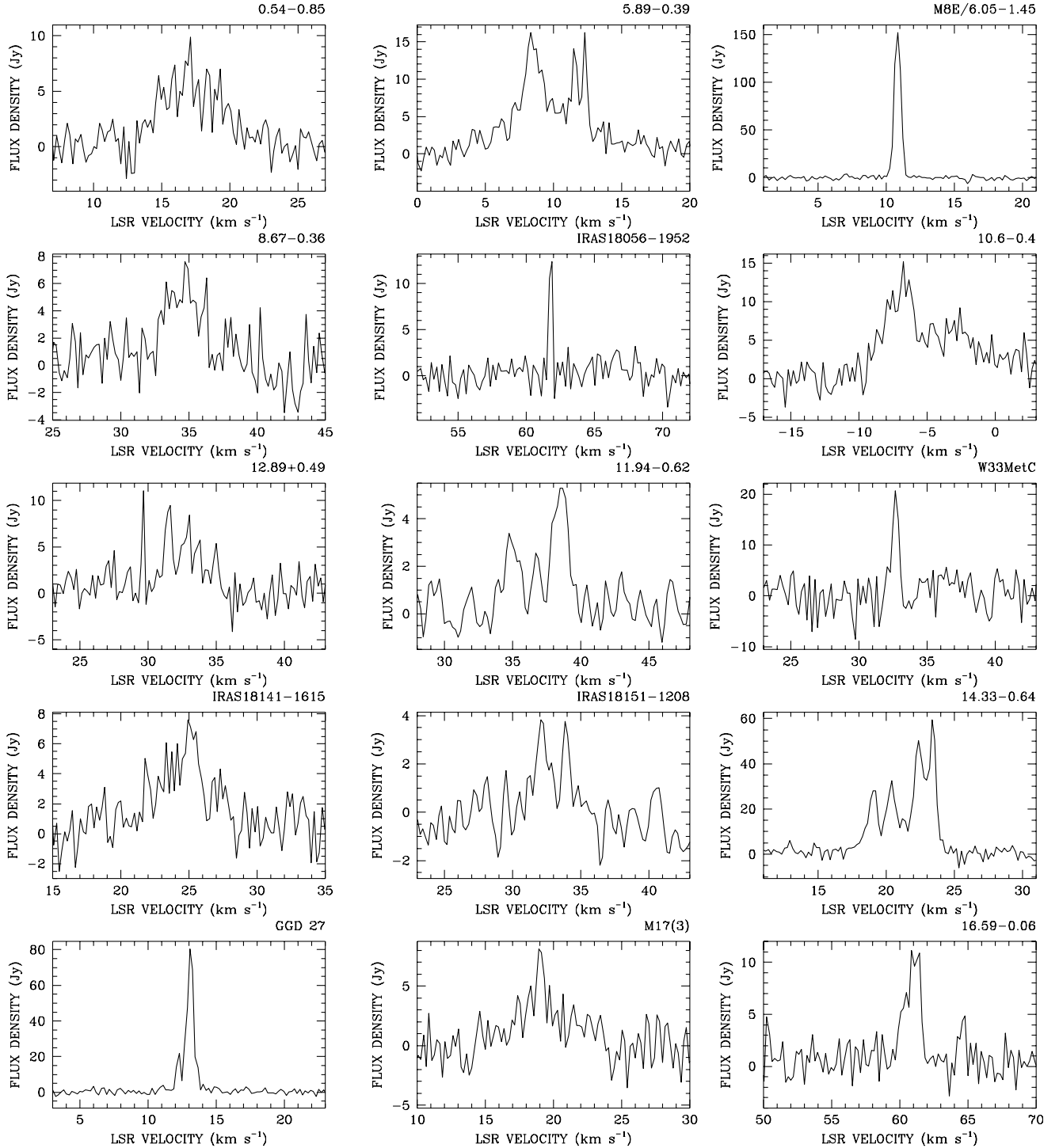
Figure 1 – *continued*

Sgr A-A. The 95-GHz spectrum of this source consists of a very broad component and possibly a weak narrow component at a velocity of $47\,\mathrm{km\,s^{-1}}$. It is almost identical to the 44-GHz spectrum (Haschick et al. 1990), with the narrow component relatively stronger at 44 GHz. A nine-point map (Fig. 8) of the source does not show the narrow component, probably because of the shorter integration time of the map spectra. The broad component is extended in declination with an angular size of 150 arcsec, and is unresolved (less than 30 arcsec) in right ascension. This is one of the rare strong thermal sources in our sample.

M8E. A single very strong narrow line is present in the 95-GHz spectrum, which is similar to that at 44 GHz. This is one of the strongest masers in both the 44- and 95-GHz transitions, and its angular extent is known to be less than 0.2 arcsec (Kogan & Slysh 1998; Slysh et al. 1999). A thorough discussion of the methanol emission from this source is given in Val'tts (1999b).

W33MetC. A single feature near $32.5\,\mathrm{km\,s^{-1}}$ is present in the
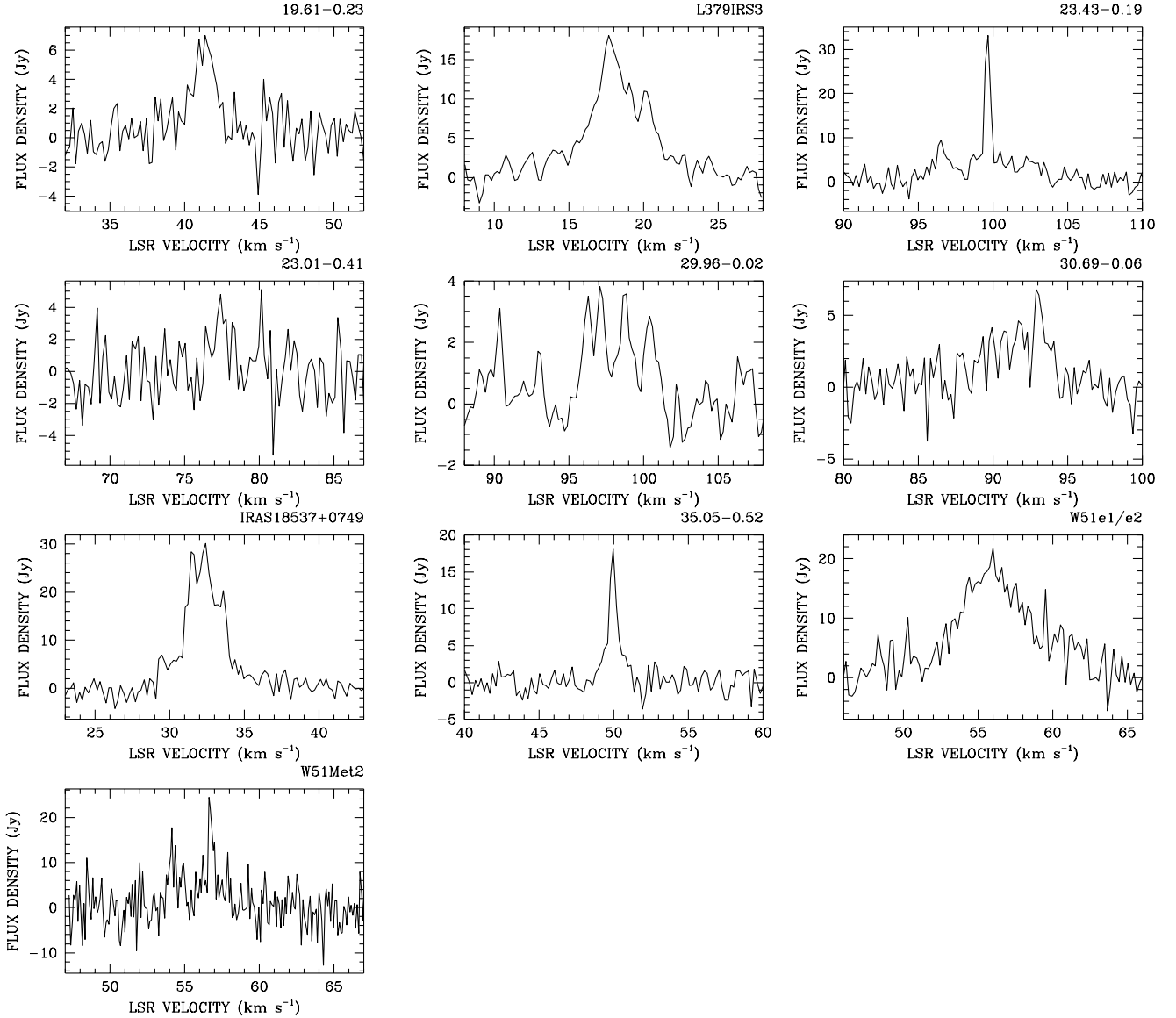
Figure 1 – *continued*

95-GHz spectrum. At 44 GHz there is also a weaker component at $36.28 \, \text{km s}^{-1}$ which is not visible in the 95-GHz spectrum. The 95-GHz emission in this source has been mapped by Pratap & Menten (1992), and the corresponding 44-GHz maser has been shown to coincide with its position (Slysh et al. 1999). A full discussion of the methanol emission from this source is given by Val'tts (1999a).

14.33−0.64. This intense class I methanol maser was discovered at 44 GHz at Parkes (Slysh et al. 1994). At 95 GHz the maser is also strong and its spectrum consists of four peaks, similar to the 44-GHz spectrum. A 44-GHz map of this maser is discussed by Slysh et al. (1999).

GGD 27. 44-GHz class I methanol maser emission in this source was discovered by Kalenskii et al. (1992), and a VLA map of it is presented by Slysh et al. (1999). At both 95 and 44 GHz the spectrum is dominated by a strong narrow feature. A nine-point map of the 95-GHz emission (Fig. 9) shows that it is strongest at a position offset in right ascension by -23 ± 8 arcsec and in declination by -8 ± 5 arcsec from the nominal position.

L379IRS3. The 44-GHz methanol maser associated with this source was also discovered by Kalenskii et al. (1992), and mapped with the VLA by Kogan & Slysh (1998) and Slysh et al. (1999). The 95-GHz spectrum is very similar to that at 44 GHz, and a map (Fig. 10) of the 95-GHz emission shows that the four spectral features are spread over an area of approximately 30 arcsec^2, similar to the 44-GHz emission.

23.43−0.19. Two Gaussian components have been fitted to the detection at 95 GHz of this source; both are present in the 44-GHz spectrum (Slysh et al. 1994). In addition there are several components near $103 \, \text{km s}^{-1}$ in the 44-GHz spectrum that are not present at 95 GHz.

IRAS 18537+0749 (S76E). This rather strong source was discovered to be a class I methanol maser during observations of the 36-GHz $4_{-1} - 3_0$ E transition at Puschino (Val'tts, private communication). In both transitions it appears that a blend of several narrow lines is producing a spectrum resembling a wide band of emission.

W51e1/e2. Only a broad component is present in our 95-GHz spectrum. The narrow spectral feature at $48.88 \, \text{km s}^{-1}$ detected by

Table 2. Sources undetected at 95 GHz.

Source	RA 1950 (h m s)	Dec. 1950 (° ′ ″)	LSR radial velocity (km s^{-1})	3σ (Jy)	Distance Near (kpc)	Distance Far (kpc)
175.84−21.48	04:16:08.98	19:17:54.9	0.00	7.4	0.1	17.1
176.23−20.87	04:19:06.98	19:25:44.9	0.00	8.0	0.1	17.1
N105	05:10:12.64	−68:57:07.8	250.70	1.6		
210.42−19.76	05:33:53.17	−06:46:49.9	10.00	9.0	1.2	15.8
205.45−14.55	05:43:35.87	−00:09:25.9	10.00	7.1	1.3	16.7
213.83+0.62	06:52:43.57	−00:27:11.0	10.00	8.3	1.1	15.2
232.62+1.00	07:29:54.97	−16:51:47.0	23.00	10.6	1.1	15.2
233.76−0.19	07:27:52.67	−18:26:08.0	43.00	5.9	4.2	14.3
243.16+0.37	07:50:18.37	−26:17:53.0	52.00	6.5	5.3	13.0
254.66+0.21	08:18:54.06	−36:03:00.0	64.00	5.8	7.2	11.7
IRAS 08337−4028	08:33:42.40	−40:28:01.8	−2.00	5.2	0.3	3.2
263.25+0.52	08:47:00.46	−42:43:15.0	13.00	6.5	2.7	4.7
IRAS 08546−4254	08:54:36.20	−42:54:06.0	9.00	2.8	2.3	4.0
IRAS 09015−4843	09:01:33.20	−48:43:25.4	56.00	4.4	8.0	
IRAS 09018−4816	09:01:50.30	−48:15:57.9	16.00	2.7	3.7	4.0
IRAS 09149−4743	09:14:54.10	−47:43:13.0	4.00	3.6	2.2	
284.35−0.42	10:22:20.00	−57:37:25.0	7.00	3.0	1.4	5.6
285.32−0.03	10:30:04.23	−57:47:50.1	0.60	2.9	0.5	5.0
IRAS 10303−5746	10:30:21.36	−57:46:44.0	1.00	3.7	0.6	5.1
IRAS 10460−5811	10:46:06.30	−58:11:12.4	−2.00	3.0	0.1	5.2
IRAS 10555−6242	10:55:34.80	−62:42:49.8	−16.00	2.6	2.4	3.5
IRAS 11097−6102	11:09:46.70	−61:02:06.0	−30.00	3.1	2.9	
291.58−0.43	11:12:58.10	−60:53:40.0	11.00	3.8	1.5	7.8
293.84−0.78	11:29:49.60	−61:58:12.5	36.90	3.5	3.9	10.7
293.95−0.91	11:30:22.70	−62:07:22.2	41.40	3.9	4.3	11.2
IRAS 11332−6258	11:33:15.00	−62:58:13.0	−10.00	3.4	0.8	6.3
298.22−0.33	12:07:16.90	−62:33:01.0	31.80	3.8	3.2	11.2
299.01+0.13	12:14:42.90	−62:12:21.0	19.00	3.8	2.0	10.2
IRAS 12272−6240	12:27:15.90	−62:40:25.0	8.00	5.6	1.0	9.6
IRAS 13080−6229	13:08:05.54	−62:29:58.1	−33.00	3.7	2.9	6.9
IRAS 13111−6228	13:11:07.49	−62:28:31.7	−37.00	4.8	3.3	6.5
308.92+0.12	13:39:35.40	−61:53:47.0	−30.00	2.7	2.3	8.4
IRAS 13504−6151	13:50:27.70	−61:51:37.3	3.00	2.9	0.4	11.4
311.96+0.14	14:04:19.70	−61:08:34.0	−30.00	3.8	2.1	9.6
IRAS 14050−6056	14:05:05.40	−60:56:29.0	−50.00	2.8	4.0	7.4
IRAS 14159−6038	14:16:00.50	−60:38:00.0	−10.00	2.5	0.6	11.1
318.05+0.09	14:49:52.91	−58:56:47.1	−49.51	3.2	3.4	9.2
318.94−0.20	14:57:01.50	−58:47:14.2	−36.10	4.1	2.5	10.4
322.17+0.62	15:14:50.20	−56:27:51.1	−53.86	3.4	3.6	9.8
326.66+0.57	15:40:59.00	−53:57:24.1	−41.23	3.4	2.8	11.4
326.662+0.521	15:41:12.87	−53:59:39.4	−41.00	4.8	2.8	11.4
327.590−0.094	15:48:45.38	−53:54:22.8	−86.30	2.4	5.4	8.9
327.945−0.115	15:50:42.65	−53:41:55.7	−51.70	2.8	3.4	11.0
328.20−0.58	15:54:02.31	−53:53:37.1	−40.79	3.5	2.8	11.7
329.339+0.148	15:56:43.74	−52:36:13.6	−106.50	2.5	7.3	
329.622+0.138	15:58:11.08	−52:25:38.2	−60.10	3.2	3.9	10.8
329.610+0.114	15:58:13.81	−52:27:12.8	−60.10	3.2	3.9	10.8
331.425+0.264	16:06:22.14	−51:08:14.9	−88.60	3.2	5.4	9.6
331.120−0.118	16:06:34.50	−51:37:31.3	−65.00	3.0	4.2	10.7
332.094−0.421	16:12:28.14	−51:10:59.6	−61.40	3.1	4.0	11.0
332.351−0.436	16:13:43.46	−51:01:00.6	−53.10	2.6	3.6	11.5
332.560−0.148	16:13:25.00	−50:39:50.1	−51.00	2.7	3.5	11.6
335.78+0.17	16:26:03.00	−48:09:44.1	−48.53	3.5	3.5	12.0
339.88−1.26	16:48:24.76	−46:03:34.0	−31.87	3.5	2.8	13.2
345.41−0.94	17:06:02.01	−41:31:44.0	−22.86	2.6	2.6	13.9
348.18−0.49	17:08:39.01	−38:27:06.0	−7.18	3.1	1.1	15.9
IRAS 17424−2859	17:42:29.00	−28:59:20.0	28.80	3.3		
IRAS 17432−2855	17:43:16.00	−28:55:05.0	51.90	2.2		
IRAS 17433−2841	17:43:21.00	−28:41:15.0	34.80	2.9		
IRAS 17470−2853	17:47:04.00	−28:53:13.0	17.30	2.6	7.4	9.6
25.53+0.38	18:33:51.38	−06:26:59.4	95.60	2.7	5.7	9.7
25.41+0.09	18:34:37.30	−06:41:42.7	97.40	2.5	5.7	9.6
25.48+0.06	18:34:53.26	−06:38:34.8	95.50	2.8	5.7	9.7
25.82−0.18	18:36:21.78	−06:27:24.2	91.70	3.1	5.5	9.8
26.57−0.25	18:38:00.13	−05:49:14.4	103.80	3.3	6.1	9.1
29.98−0.04	18:43:35.00	−02:42:19.0	102.60	3.0	6.4	8.3
IRAS 18449−0115	18:44:59.00	−01:15:59.0	97.80	6.4	6.3	8.3
IRAS 18469−0132	18:46:59.00	−01:32:38.0	84.60	2.6	5.3	9.2

Table 3. Comparison between Mopra and Onsala observations of 95-GHz sources.

Source name	Mopra LSR radial velocity (km s^{-1})	Line width (km s^{-1})	Flux density (Jy)	Onsala LSR radial velocity (km s^{-1})	Line width (km s^{-1})	Flux density (Jy)
OMC-2	11.4	0.3	138(7.0)	11.4	1.1	69.9(1.1)
NGC 2264	7.3	0.2	99.2(5.7)	7.7	1.0	46.2(1.7)
W33MetC	32.7	0.5	21.2(3.1)	32.3	1.6	12.6(1.8)
L379IRS3	18.0	2.7	10.1(1.2)	18.2	3.9	21.3(1.3)
W51e1/e2	55.9	5.3	17.7(0.5)	55.9	9.5	21.8(2.0)
W51Met2	56.7	0.6	19.7(2.6)	56.5	1.2	9.4(0.9)
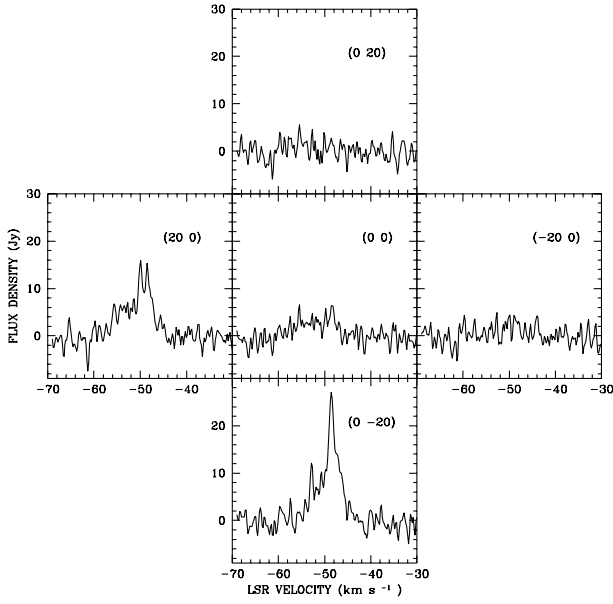
Figure 2. Map of 333.13−0.43.
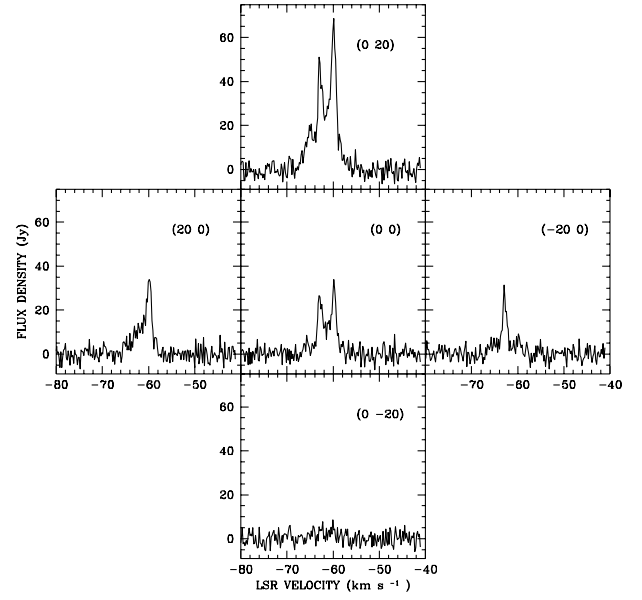
Figure 4. Map of 338.92+0.56.
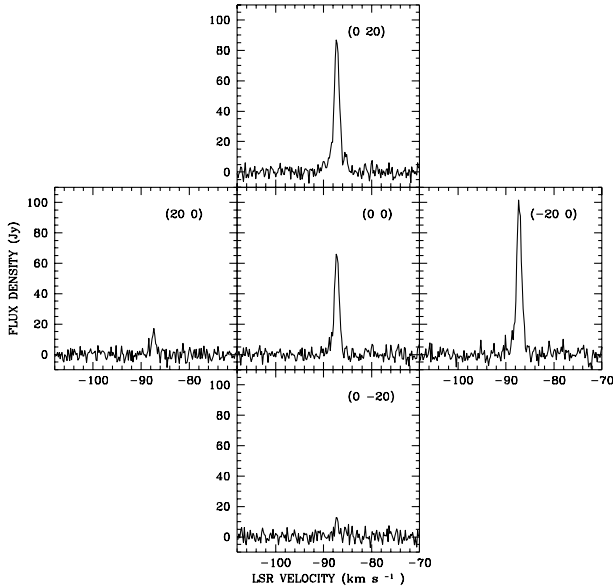
Figure 3. Map of 333.23−0.05.
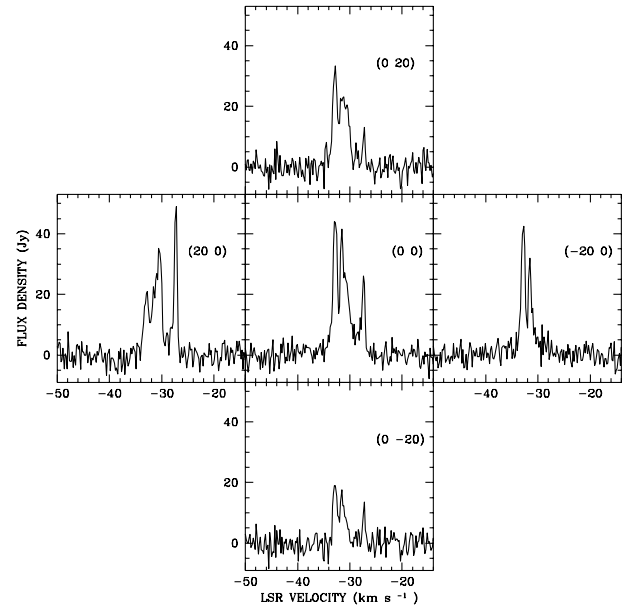
Figure 5. Map of 343.12−0.06.
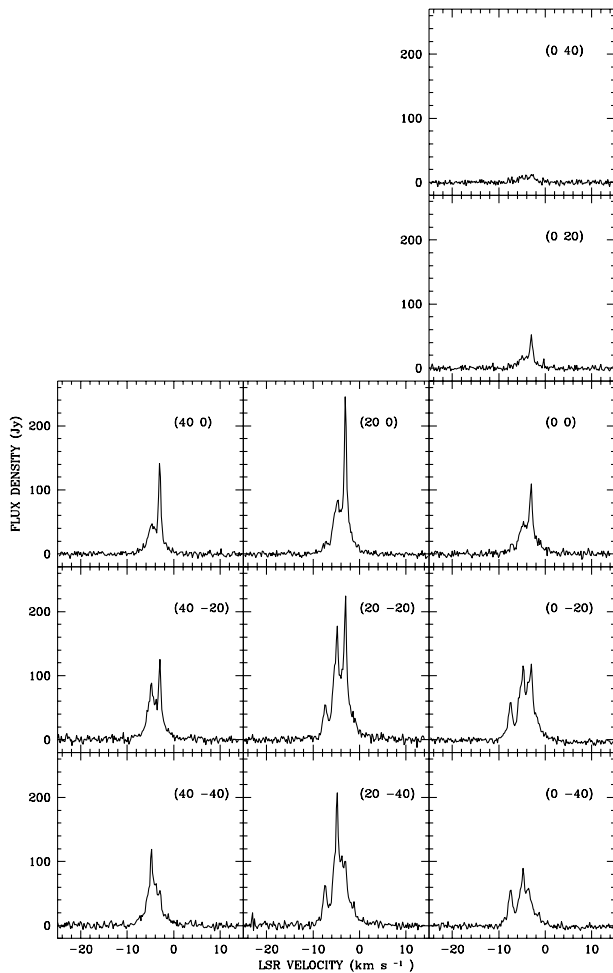
Figure 6. Map of NGC 6334I(N).

Table 4. Positions of components in NGC 6334I(N).

N	LSR radial velocity (km s^{-1})	Line width (km s^{-1})	$\Delta\alpha$ ($''$)	$\Delta\delta$ ($''$)	Flux density (Jy)
1	−7.5	0.8	9(5)	−30(5)	44
2	−4.8	0.8	18(1)	−35(5)	110
3	−4.0	4.0	18(5)	−28(5)	100
4	−3.0	0.5	24(6)	−12(7)	175

Haschick et al. (1990) at 44 GHz is not visible in the 95-GHz spectrum, because it is shifted from W51e1/e2 by about 70 arcsec and was outside the main beam of the Mopra telescope (Pratap & Menten 1992).

4   DISCUSSION

The spectra of the 95-GHz $8_0 - 7_1$ A$^+$ methanol emission sources found in this survey are in general similar to the spectra of the corresponding 44-GHz $7_0 - 6_1$ A$^+$ sources. The emission in the two transitions typically covers the same velocity range, has approximately the same number of spectral features with very similar radial velocities, and in some cases even has the same relative intensities of the components. In Table 5 we list the single strongest feature in each spectrum at 95 GHz and the corresponding
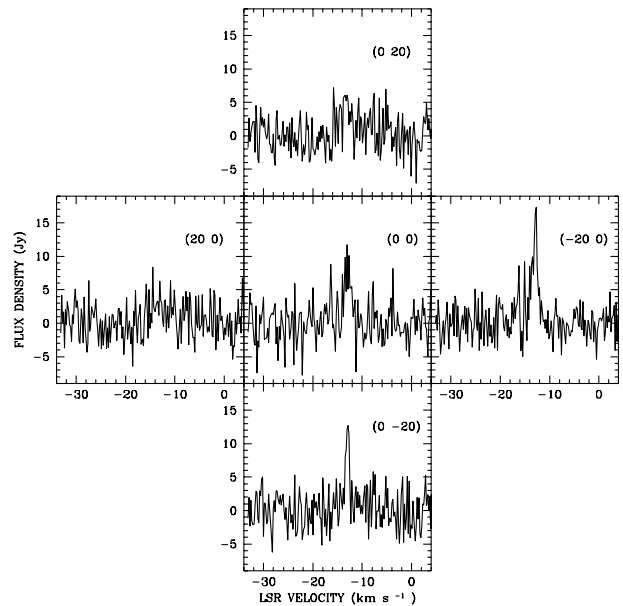
Figure 7. Map of 351.64−1.26.

spectral features at 44 GHz of the sources detected by Slysh et al. (1994). One can see that there is always a corresponding spectral feature at 44 GHz to every 95-GHz spectral feature from Table 5, and their radial velocities agree in general to within 0.1 km s^{-1}. The linewidth of the 95-GHz components is in general somewhat larger than the linewidth of the corresponding 44-GHz features, partly owing to a lower spectral resolution in the 95-GHz observations, but nevertheless there are many very narrow 95-GHz features with a linewidth less than 1 km s^{-1}. The peak flux density of the 95-GHz components is generally lower than the flux density of the 44-GHz features. Fig. 11 shows a comparison between the flux densities of spectral features with the same radial velocities from the two transitions. In constructing this plot, data on all available sources were used, including the results of this work and of the observations at Onsala (Val'tts et al. 1995). The straight line (with a correlation coefficient $r = 0.73$) shows the best-fitting linear dependence which was found to be

$$S(95) = (0.32 \pm 0.08) \times S(44) - (8.1 \pm 2.7). \tag{1}$$

Although the scatter is quite large, on average the 95-GHz methanol masers are a factor of 3 weaker than the 44-GHz masers. This result is consistent with the findings of Val'tts et al. (1995), who found a linear dependence between the integrated fluxes at the two frequencies. We have used peak flux densities rather than luminosities since our survey is flux density limited by the sensitivity of the instrument, and luminosities would give a spurious correlation owing to the multiplication of the flux densities at the two frequencies by the same distance squared. The slope of the dependence between the integrated flux densities found by Val'tts et al. (1995) is 0.52 ± 0.05, which is larger than the slope of 0.32 ± 0.08 found in this paper for the peak flux densities. This difference may be due to the larger average linewidth of the 95-GHz masers mentioned above. The correlation between the peak flux densities and the observed similarity in the spectra of the two transitions is strong evidence in favour of the suggestion that the emission from both transitions arises from the same spatial location. A comparison of published high-resolution maps of the 44- and 95-GHz class I methanol masers in
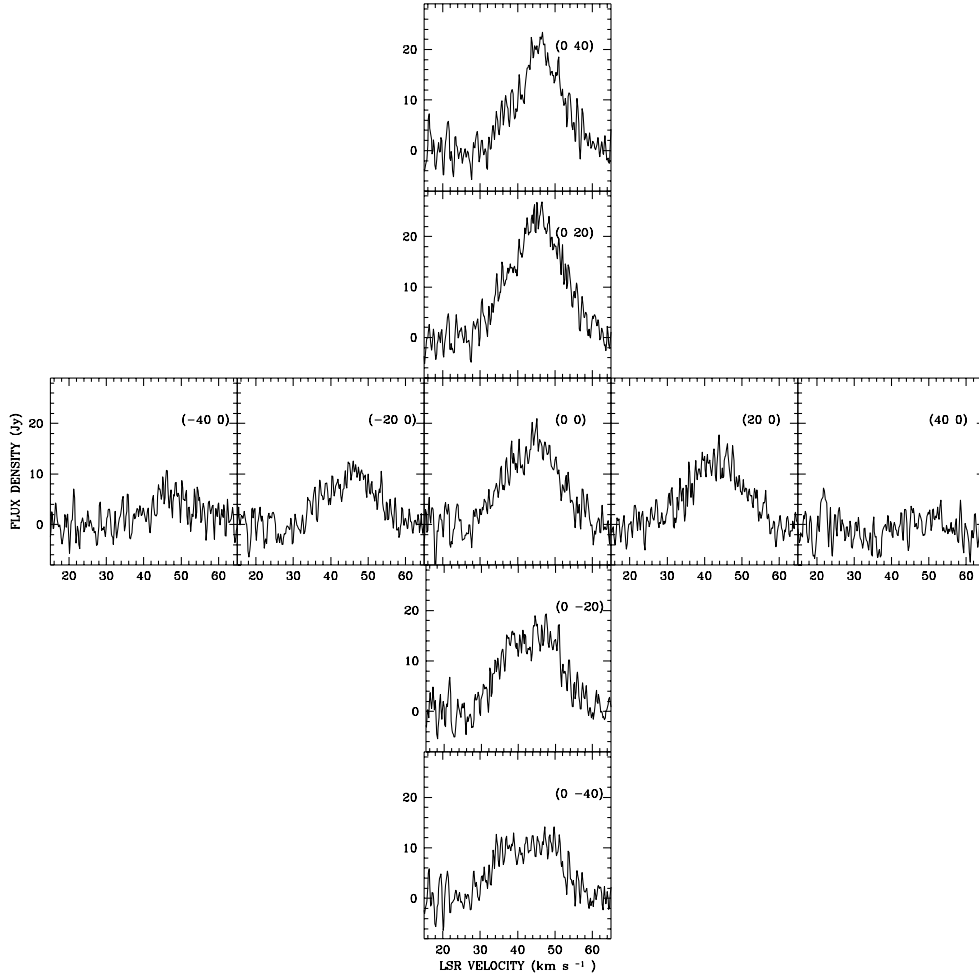
Figure 8. Map of Sgr A-A.

DR21(OH) and W33MetC shows that their images are very alike and consist of the same number of isolated maser spots (Plambeck & Menten 1990; Pratap & Menten 1992; Kogan & Slysh 1998; Slysh et al. 1999), consistent with this hypothesis.

The two transitions belong to the class I methanol masers (Menten 1991), which are thought to be pumped through collisional excitation. The difference between the two transitions is that the upper level of the 95-GHz $8_0 - 7_1$ A^+ transition is 18.5 K above the upper level of the 44-GHz $7_0 - 6_1$ A^+ transition. Therefore the population of the former is expected to be lower than the population of the latter, resulting in the lower intensity of 95-GHz emission compared with the intensity of the 44-GHz transition, although it is difficult to estimate the difference without any knowledge of the kinetic temperature and particle density in the source.

We used a large velocity gradient (LVG) code to calculate the intensity ratios of the $7_0 - 6_1$ A^+ and $8_0 - 7_1$ A^+ transitions in a collisional excitation model for four different parameter sets. The model parameters and the intensity ratios are presented in Table 6. The collisional selection rules are based on the paper by Lees & Haque (1974), and imply that $\Delta K = 0$ collisions are preferred by a factor of 4. For model 1 with a gas temperature of 20 K and density of 0.56×10^5 cm^{-3}, the ratio of the 44- and 95-GHz intensities is 3.3, i.e. close to the mean observed ratio. The 95-GHz intensity is

lower owing to the lower population of the 8_0 A^+ level relative to that of the 7_0 A^+ level, and because of a weaker inversion at 95 GHz. Increasing either the gas temperature or the density decreases the model ratio below the observed value. Thus our results favour class I maser model with a gas temperature of about 20 K and a density of less than 10^6 cm^{-3}.

5 SUMMARY

(1) As a result of a survey in the southern hemisphere, 85 methanol emission sources were detected in the $8_0 - 7_1$ A^+ transition at 95 GHz. This survey, together with a similar Onsala survey, (Val'tts et al. 1995), completes a whole-sky survey of methanol emission at 95 GHz.

(2) Most of the detected sources are class I methanol masers, and the majority of them have counterparts in other class I methanol transitions, such as the $7_0 - 6_1$ A^+ transition at 44 GHz.

(3) The previously found correlation between the methanol maser emission intensities at 44 and 95 GHz is confirmed here, using a larger sample of sources.

(4) A maser model with collisional excitation based on LVG calculations can explain the observed intensity ratio at 44 and 95 GHz, and gives constraints on the temperature and particle density.
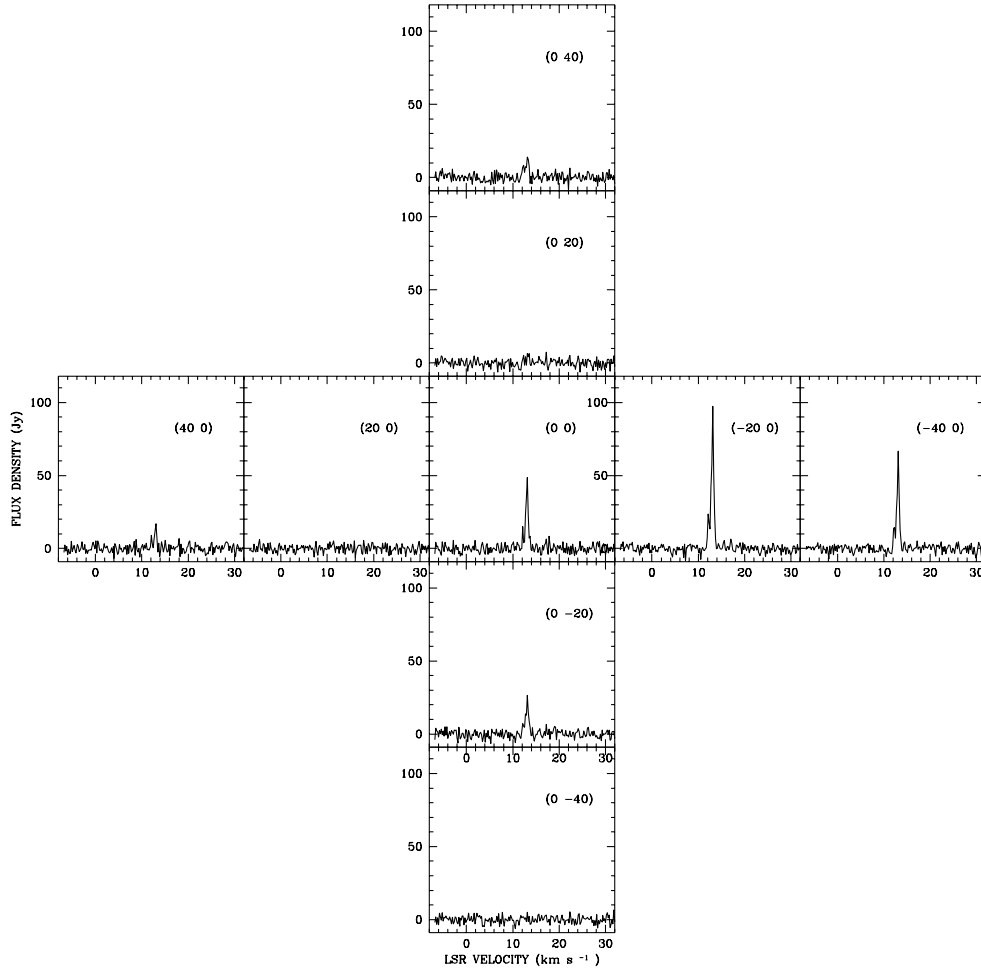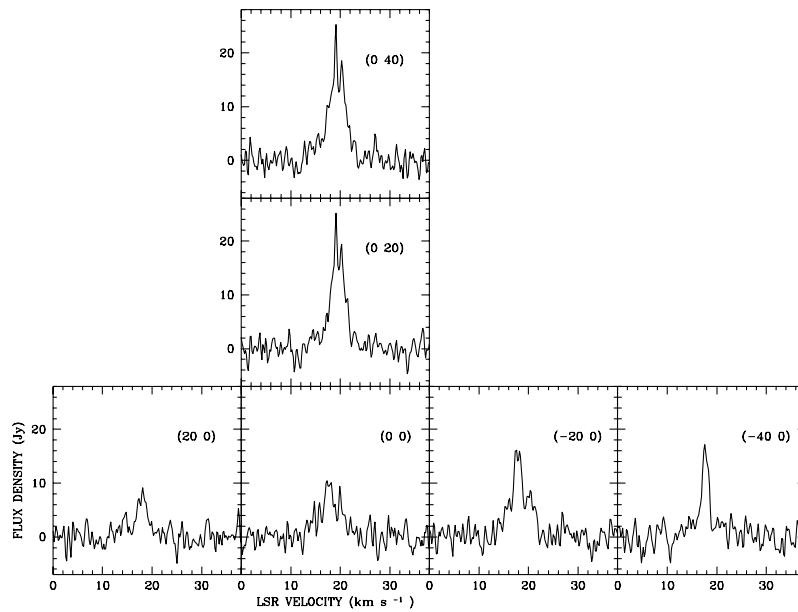
Figure 9. Map of GGD 27.

Figure 10. Map of L379IRS3.

Table 5. Comparison between Mopra and Parkes observations of 44-GHz sources.

| Source name	Mopra LSR radial velocity (km s^{-1})	Mopra Line width (km s^{-1})	Mopra Flux density (Jy)	Parkes LSR radial velocity (km s^{-1})	Parkes Line width (km s^{-1})	Parkes Flux density (Jy)
269.20−1.13	9.4	0.7	15.1(2.3)	9.4	0.3	23.2(1.6)
270.26+0.84	9.3	0.6	7.0(3.1)	9.7	0.3	37.0(6.3)
294.97−1.73	−8.2	1.3	5.9(0.8)	−8.25	0.9	12.2(2.0)
305.21+0.21	−42.3	0.6	26.1(2.0)	−42.3	0.5	75.7(3.7)
305.36+0.20	−33.4	0.9	17.4(1.4)	−33.1	0.6	106(8.9)
316.76−0.02	−39.4	0.7	12.9(1.6)	−39.3	0.4	26.9(2.2)
320.28−0.31	−66.3	0.7	14.5(1.9)	−66.3	0.9	45.4(3.2)
323.74−0.27	−49.8	2.9	4.9(0.4)	−49.9	0.4	23.1(4.2)
324.72+0.34	−50.6	2.5	3.1(0.5)	−51.8	0.4	43.8(3.7)
327.29−0.58	−44.6	2.5	14.3(1.1)	−44.3	0.9	26.1(3.1)
328.81+0.64	−40.9	3.1	7.2(0.9)	−40.6	1.2	23.5(1.6)
328.24−0.55	−41.2	1.8	7.3(0.4)	−41.1	0.3	11.8(2.2)
329.03−0.21	−43.7	1.3	19.3(1.3)	−43.7	0.7	24.9(3.5)
331.13−0.25	−91.0	1.0	20.5(0.7)	−91.0	0.7	95.0(4.4)
331.34−0.35	−65.7	0.7	15.8(1.3)	−65.7	0.4	24.0(5.5)
333.23−0.05	−87.2	1.3	99.3(2.3)	−87.2	1.3	205(6.6)
333.13−0.43	−48.6	1.0	17.0(2.1)	−48.2	0.8	98.5(3.8)
333.61−0.22	−49.7	2.9	3.0(0.4)	−49.3	0.6	21.2(2.5)
335.59−0.29	−45.5	0.6	22.3(2.2)	−45.4	0.6	158(4.5)
336.41−0.26	−87.6	0.7	24.8(0.9)	−87.6	0.7	51.4(3.7)
337.40−0.41	−42.3	0.2	16.5(2.4)	−42.3	0.2	26.8(2.3)
338.92+0.56	−62.7	1.8	43.3(1.9)	−62.9	0.5	166(5.4)
337.91−0.47	−43.6	0.4	58.2(2.4)	−43.4	0.4	273(4.0)
341.19−0.22	−42.0	0.7	6.1(0.9)	−41.9	0.3	92.9(2.9)
341.22−0.21	−43.8	1.8	15.6(1.0)	−43.8	0.4	25.5(6.8)
345.01+1.79	−13.1	0.5	49.6(1.9)	−13.2	0.4	33.4(2.7)
343.12−0.06	−32.8	0.8	46.6(3.0)	−32.8	1.0	71.9(2.2)
344.23−0.57	−20.3	0.6	33.2(1.9)	−20.3	0.6	48.4(9.6)
345.51+0.35	−16.5	0.9	3.2(0.5)	−16.5	0.6	16.2(1.6)
345.00−0.22	−28.0	0.7	23.5(1.4)	−27.9	0.6	69.3(9.4)
349.10+0.11	−78.0	0.5	6.4(1.6)	−77.9	0.3	23.8(2.1)
351.16+0.70	−4.9	0.6	26.3(3.3)	−4.5	0.4	36.9(9.9)
351.24+0.67	−4.5	3.4	4.3(0.4)	−4.5	0.3	21.5(0.8)
351.41+0.64	−8.2	4.2	20.2(1.0)	−8.4	1.4	39.9(1.9)
351.78−0.54	−6.9	0.4	73.0(2.3)	−6.9	0.4	150(4.6)
351.64−1.26	−12.7	0.7	15.2(2.5)	−13.1	1.2	12.7(1.1)
354.61+0.47	−17.9	0.5	24.0(1.7)	−17.8	0.5	55.5(9.8)
353.41−0.36	−16.6	0.6	8.1(0.8)	−16.5	0.6	31.4(3.5)
359.62−0.25	19.3	0.6	15.9(1.1)	19.4	0.4	105(5.2)
0.54−0.85	16.9	0.6	4.0(0.9)	14.8	0.7	33.8(1.7)
M8E	11.0	0.5	129.7(2.0)	10.9	0.4	510(34.2)
12.89+0.49	31.5	0.4	5.7(1.1)	31.4	0.3	24.4(2.2)
14.33−0.64	23.4	0.5	52.8(2.9)	23.5	0.5	120(9.8)
16.59−0.06	61.3	0.8	9.8(1.6)	61.2	0.2	12.5(2.5)
23.43−0.19	99.6	0.5	33.6(2.1)	99.7	0.4	78.9(6.1)
23.01−0.41	77.4	1.3	3.4(0.6)	77.1	0.3	32.2(2.8)
30.69−0.06	89.3	0.6	3.8(0.6)	89.5	0.5	29.8(7.7)
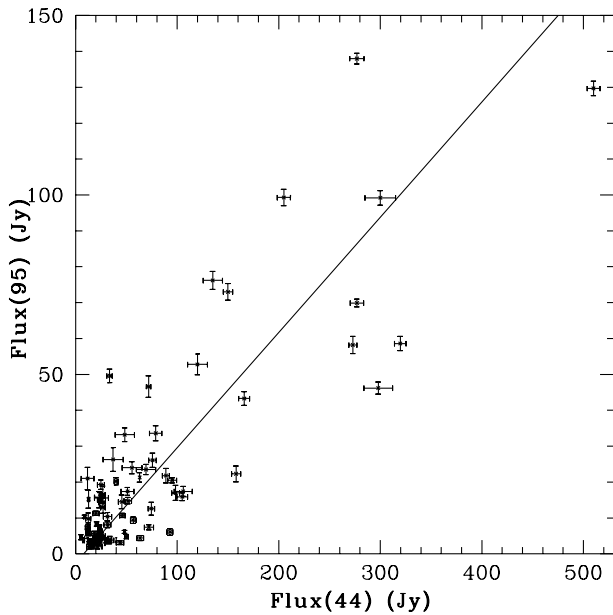
Figure 11. A correlation between 95- and 44-GHz peak flux densities. The straight line is a best fit: $y = (0.32 \pm 0.08)x - (8.1 \pm 2.7)$, correlation coefficient $r = 0.73$.

Table 6. LVG calculation results: ratios of 44/95 intensities for four models. Methanol density, divided by velocity gradient, for all models is 0.67×10^{-2} cm^{-3} (km s^{-1} pc^{-1})$^{-1}$.

Model	T_{kin} (K)	n_{H_2}	44/95 GHz intensity ratio
1	20	0.56E+5	3.3
2	50	0.56E+5	1.7
3	100	0.56E+5	0.4
4	20	0.56E+6	1.2

REFERENCES

Bachiller R., Menten K. M., Gómez-González J., Barcia A., 1990, A&A, 240, 116
Brand J., Blitz L., 1993, A&A, 275, 67
Caswell J. L., Vaile R. A., Ellingsen S. P., Whiteoak J. B., Norris R. P., 1995, MNRAS, 272, 96
Cragg D. M., Johns K. P., Godfrey P. D., Brown R. D., 1992, MNRAS, 259, 203
De Lucia F. C., Herbst E., Anderson T., Helminger P., 1989, J. Mol. Spectrosc., 134, 395
Ellingsen S. P., von Bibra M. L., McCulloch P. M., Norris R. P., Deshpande A. A., Phillips C. J., 1996, MNRAS, 280, 378
Genzel R., Stutzki J., 1989, ARA&A, 27, 41
Haschick A. D., Menten K. M., Baan W. A., 1990, ApJ, 354, 556
Houghton S., Whiteoak J. B., 1995, MNRAS, 273, 1033
Kalenskii S. V., Bachiller R., Berulis I. I., Val'tts I. E., Gómez-González J., Martin-Pintado J., Rodriguez-Franco A., Slysh V. I., 1992, AZh, 69, 1002
Kalenskii S. V., Liljestrom T., Val'tts I. E., Vasil'kov V. I., Slysh V. I., Urpo S., 1994, A&AS, 103, 129
Kogan L., Slysh V. I., 1998, ApJ, 497, 800
Kutner M. L., Ulich B. L., 1981, ApJ, 250, 341
Lees R. M., Haque S. S., 1974, Can. J. Phys., 52, 2250
Menten K. M., 1991, in Haschick A. D., Ho P. T. P., eds, ASP Conf. Ser. Vol. 16, Skylines, Proc. Third Haystack Observatory Conference on Atoms, Ions and Molecules. Astron. Soc. Pac., San Francisco, p. 119
Morimoto M., Ohishi M., Kanagawa T., 1985, ApJ, 288, L11
Neckel T., 1978, A&A, 69, 51
Norris R. P., Whiteoak J. B., Caswell J. L., Wieringa M. H., Gough R. G., 1993, ApJ, 412, 222
Plambeck R. L., Menten K. M., 1990, ApJ, 364, 555
Pratap P., Menten K. M., 1992, in Clegg A. E., Nedoluha G. E., eds, Lecture Notes in Physics, Astrophysical Masers, Vol. 412. Springer Verlag, Berlin, p. 211
Slysh V. I., Kalenskii S. V., Val'tts I. E., Otrupcek R., 1994, MNRAS, 268, 464
Slysh V. I., Val'tts I. E., Kalenskii S. V., Golubev V. V., 1999, Astron. Rep., 43, 785
Sung H., Bessell M. S., Lee S., 1997, AJ, 114, 2644
Thronson H. A. Jr, Lowenstein R. F., Stokes G. M., 1979, AJ, 84, 1328
Val'tts I. E., 1998, Astron. Lett., 24, 788
Val'tts I. E., 1999a, Astron. Rep., 43, 148
Val'tts I. E., 1999b, Astron. Rep., 43, 157
Val'tts I. E., Dzura A. M., Kalenskii S. V., Slysh V. I., Booth R. S., Winnberg A., 1995, AZh, 72, 22
Val'tts I. E., Ellingsen S. P., Slysh V. I., Kalenskii S. V., Otrupcek R., Voronkov M. A., 1999, MNRAS, 310, 1077
Walsh A. J., Hyland A. R., Robinson G., Burton M. G., 1997, MNRAS, 291, 261

This paper has been typeset from a TEX/LATEX file prepared by the author.